Received Date : 04-May-2015

Accepted Date : 11-Sep-2015

Article type : Article

Contributing Editor: Elizabeth Dickey

Corresponding Author mail-id: ericonium@gmail.com

ZrB_2–ZrC_xN_{1-x} eutectic composites produced by melt-solidification

Eric Jianfeng Cheng,[†,‡,§] Hirokazu Katsui,[‡] Takashi Goto[†,‡]

[‡]Institute for Materials Research, Tohoku University, 2-1-1, Katahira, Aoba-ku, Sendai 980-8577, Japan

[§]Department of Mechanical Engineering, University of Michigan, 2350 Hayward, G.G. Brown Laboratory, Ann Arbor, MI 48109, USA

Abstract: Ceramic eutectics are naturally occurring *in-situ* composites and can offer superior mechanical properties. Here, ZrB_2–ZrC_xN_{1-x} quasi-binary ceramic eutectic composites were produced by arc-melting a mixture of ZrB_2, ZrC and ZrN powders in an N_2 atmosphere. The arc-melted ZrB_2–ZrC_xN_{1-x} composites containing 50 mol% of ZrB_2 (irrespective of the ZrC/ZrN ratio) showed rod-like eutectic structures, where ZrC_xN_{1-x} single-crystalline rods were dispersed in the ZrB_2 single-crystalline matrices. Multiple orientation relationships between the ZrC_xN_{1-x} rods and the ZrB_2 matrices were observed, and one was determined as ZrB_2 $\{01\bar{1}0\}$//ZrC_xN_{1-x} $\{111\}$ and ZrB_2 $< 2\bar{1}\bar{1}0 >$//ZrC_xN_{1-x} $< 10\bar{1} >$. The rod-like eutectic composites had higher hardness than the hypo- and hypereutectic composites and the $50ZrB_2$–40ZrC–10ZrN (mol%) eutectic composite showed the highest Vickers hardness (H_v) of 19 GPa.

Keywords: ZrB_2–ZrC_xN_{1-x}; Eutectic composites; Rod-like structure; Crystal orientation; Vickers hardness

1. Introduction

ZrB_2, ZrC and ZrN are members of a family of materials known as ultra high-temperature ceramics (UHTCs).[1] The melting temperatures of ZrB_2, ZrC and ZrN are about 3520 K, 3970 K and 3170 K, respectively.[2] Besides high melting temperatures, the Zr-based compounds also offer an excellent combination of chemical stability, high electrical and thermal conductivities, low density and high thermal shock resistance.[2-5] As naturally occurring *in-situ* composites, ceramic eutectics can combine the properties of two or more components and possess superior mechanical properties, such as higher wear resistance and better fracture toughness, to the monolithic materials.[6-9] Sorrel *et al*. reported a directionally solidified ZrB_2–ZrC lamellar eutectic composite, which showed higher hardness, higher fracture toughness, and better wear resistance than the monolithic ZrB_2 and ZrC.[10] Chen *et al*. synthesized a LaB_2–ZrB_2 rod-like eutectic composite that exhibited higher hardness and fracture toughness in comparison with the individual components of LaB_2 and ZrB_2.[11] Hence, the ZrB_2–ZrC–ZrN ceramic composites could take the advantage of the physical and mechanical properties of ZrB_2, ZrC and ZN, and would be promising materials for re-entry and hypersonic vehicles, where resistance to corrosion, wear and oxidation is demanded.[4]

ZrB_2 has a hexagonal crystal structure, while ZrC and ZrN share the same face-centered cubic crystal structures.[1-2] The ZrB_2–ZrC and ZrB_2–ZrN both are quasi-binary eutectic systems, and the ZrC–ZrN is a complete solid solution system of ZrC_xN_{1-x}.[12-14] Therefore, the ZrB_2–ZrC–ZrN is expected to be a quasi-binary eutectic system of ZrB_2–ZrC_xN_{1-x}. By now, however, no research has been reported on the synthesis of ZrB_2–ZrC_xN_{1-x} quasi-binary eutectic composites. A similar ternary system, TiB_2–TiC–TiN, has been reported to be a quasi-binary eutectic system of TiB_2–TiC_xN_{1-x}.[15]

Because of strong covalent bonding and low-self diffusion coefficients of elements in the transition metal borides, carbides and nitrides, synthesis of these transition metal-based ceramic composites with high density would require long exposures to high temperatures.[16] The melt-solidification process was useful for consolidating high-melting-point materials to produce fully dense composites.[15,17] In addition, self-assembled structures by eutectic reactions could improve the mechanical properties of the constituent materials.[7-8] In this

study, *in-situ* ZrB_2–ZrC–ZrN composites were produced by arc-melting a mixture of ZrB_2, ZrC and ZrN powders in an N_2 atmosphere, and the microstructures, mechanical properties and crystal orientation relationships between phases of the produced eutectic composites were investigated.

2. Experimental Procedure

The starting materials used in this study were ZrB_2 powder (C < 0.50, O < 1.50, N < 0.50 (wt%), 1.5–2.5 μm, Kojundo Chemical Laboratory, Japan), ZrC powder (95%, 2.5 μm, Kojundo Chemical Laboratory, Japan), and ZrN powder (98%, Kojundo Chemical Laboratory, Japan). The compositions in this study were expressed as nominal mole percentages of ZrB_2, ZrC and ZrN. The nominal compositions of the prepared composites are shown in Fig. 1, in which each dot corresponds to one nominal composition. The powders of ZrB_2, ZrC and ZrN were ball-milled with ZrO_2 balls in a small amount of ethanol, and ball-milled for 4 h in a polyethylene bottle. The mixed powders were dried at 333 K for 12 h, and isostatically pressed into disks (10 mm in diameter and 3 mm in thickness) under a pressure of 5 MPa. The pressed powder disks were melted twice by an arc-melting technique in an N_2 atmosphere at 80 kPa and solidified on a water-cooled copper hearth. N_2 gas was introduced to prevent the possible dissociation of ZrN during melting process. The specimens were polished with a series of diamond grits, with a final polish using a 1 μm diamond slurry. The crystallographic phases were examined using X-ray diffraction (XRD, Ultima IV, Rigaku, Japan) with Cu Kα radiation. The microstructures of the composites were investigated by scanning electron microscopy (SEM, Hitachi: S-3100H, Japan) at 10 kV and transmission electron microscopy (TEM, EM-002B, TOPCON, Tokyo, Japan). Electron probe microanalysis (EPMA) was carried out on an electron probe microanalyzer with a TSL solutions camera control system (JXA-8621MX, JEOL, Japan). Vickers hardness was determined from 10 indentation measurements. Crystal structure illustrations were produced using the VESTA software.[18]

3. Results and Discussion

Figure 2 shows the XRD pattern of the arc-melted 50ZrB_2–30ZrC–20ZrN (mol%) composite. Reflection peaks relating to ZrB_2 and ZrC_xN_{1-x} were observed, indicating that ZrC and ZrN formed solid solutions of ZrC_xN_{1-x}. Based on XRD results, all the other arc-melted composites comprised ZrB_2 and ZrC_xN_{1-x} two phases, irrespective of the ZrC and ZrN contents. Hence, the ZrB_2–ZrC–ZrN was a quasi-binary system, consisting of ZrB_2 and ZrC_xN_{1-x} two phases.

Figure 3 presents the secondary electron SEM micrographs of the arc-melted ZrB_2–ZrC–ZrN composites, in which two phases are observed: the gray phase ZrC_xN_{1-x} and the black phase ZrB_2. For the nominal composition of 30ZrB_2–50ZrC–20ZrN (mol%), the arc-melted ZrB_2–ZrC_xN_{1-x} composite showed a hypoeutectic structure, comprising the dark-contrast ZrB_2 phase and the gray-contrast primary ZrC_xN_{1-x} phase, as shown in Fig. 3(a). The composite of 40ZrB_2–40ZrC–20ZrN (mol%) had a labyrinth-like eutectic structure (Fig. 3(b)). With increasing ZrB_2 content, elongated ZrB_2 formed as the primary phase as shown in Figs. 3(c) and (d), and the two compositions of 60ZrB_2–20ZrC–20ZrN and 80ZrB_2–10ZrC–10ZrN (mol%) were hypereutectic. Rod-like eutectic structures were locally observed in Figs. 3(a) and (c).

On the other hand, the composites with nominal compositions of 50 mol% of ZrB_2, irrespective of the ZrC/ZrN (C/N) ratio, showed rod-like eutectic structures, where the gray ZrC_xN_{1-x} rods were uniformly dispersed in the black ZrB_2 matrix, as shown in Fig. 4. As indicated by the dash-lined hexagon in Fig. 4(a), the ZrC_xN_{1-x} rods are hexagonally ordered. The diameter of the ZrC_xN_{1-x} rods slightly increased with increasing C/N ratio. Since ZrC had higher melting temperature (3970 K) than ZrN (3170 K), the melting temperature of ZrC_xN_{1-x} would be expected to increase with increasing C/N ratio. Consequently, the crystal growth rate of ZrC_xN_{1-x} would be affected, which could have resulted in the larger diameter of the ZrC_xN_{1-x} rods. The lattice parameter of ZrC (0.4691 nm) was larger than that of ZrN (0.4600 nm),[19-20] the lattice parameter of ZrC_xN_{1-x} would increase linearly with increasing C/N ratio. The change of the lattice parameter of ZrC_xN_{1-x} could be another factor associated with the change of the diameter of the ZrC_xN_{1-x} rods. The area ratio of the gray ZrC_xN_{1-x} phase in Fig. 4 (d) was about 43% (that for Figs. 4 (a), (b) and (c) was 44%, 39% and 42%, respectively), from which ZrC_xN_{1-x} was estimated to be 48 mol% in the

composite. This mole percentage of ZrC_xN_{1-x} was lower than the total mole percentages of ZrC and ZrN in the starting powders (50 mol%). The discrepancy between the nominal eutectic compositions and the compositions that yielded rod-like eutectic structures was probably a consequence of preferential vaporization of ZrN powder during arc-melting process.[21]

The most commonly observed growth morphologies of eutectic composites were lamellae (alternating parallel platelets of the two eutectic phases) and rods (fibers of one phase distributed continuously in a matrix phase).[22-23] The ZrB_2–ZrN eutectic composite with a eutectic composition of $47.5ZrB_2$–$52.5ZrN_{0.9}$ (mol%) showed a rod-like structure,[13] similar to the structures of the ZrB_2-ZrC_xN_{1-x} eutectic composites in this study. However, the directionally solidified ZrB_2–ZrC eutectic composite with a eutectic composition of $48ZrB_2$–$52ZrC_{0.9}$ (mol%) was reported to have a lamellar structure.[21] Andrea *et al*. argued that the lamellar growth was most stable at the eutectic composition, and the spatially periodic structure were stable in a range of spacings, which was limited by dynamical instabilities.[22] A zigzag instability (classical transverse phase-diffusion instability) was considered to be the first instability to occur and lead to the breakup of the lamellae into rods or labyrinth structures (depending on the initial spacing and the volume fractions of the eutectic phases).[22] Liu *et al*. experimentally proved that lamellar-rod transition could occur over a range of compositions and the instability of a lamella initiated locally through the formation of a sinusoidal perturbation.[23] In addition, the instabilities in adjacent lamellae were observed to be out of phase, leading to the hexagonal arrangement of the rods during the lamellar-to-rod transition.[23] It could be noted that the floating zone-meted $48ZrB_2$–$52ZrC_{0.9}$ (mol%) eutectic composite prepared by Sorrell *et al*. was not highly lamellar and a lamellar-to-rod morphology transition could occur as a consequence of different solidification conditions.[21] The formation of the hexagonally ordered ZrC_xN_{1-x} rods in the current study could be caused by the lamellar-to-rod transition (driven by the instabilities in adjacent lamellae) as that observed by Liu *et al*. in the Au–Cu eutectic system.[23] The instabilities of eutectic growth would vary with solidification parameters. For the intensively studied eutectic ceramic oxide system of Al_2O_3–ZrO_2, a rod-like eutectic

structure formed when prepared by a Bridgman technique,[24] while a lamellar eutectic structure occurred when produced by a high velocity CO_2 laser melting technique.[25]

A backscattered electron SEM micrograph of the $50ZrB_2$–$30ZrC$–$20ZrN$ (mol%) composite with a rod-like eutectic structure is presented in Fig. 5. There were two contrasts in the micrograph, where the phase with bright contrast was ZrC_xN_{1-x} and the phase with dark contrast was ZrB_2. EPMA analysis further confirmed that the matrix was ZrB_2 and the dispersoid was ZrC_xN_{1-x}.

Figure 6 presents a bright-field TEM image of the transverse section of the ZrB_2–ZrC_xN_{1-x} rod-like eutectic structure (a), the corresponding selected area electron diffraction (SAED) patterns of the ZrC_xN_{1-x} rods (dark phase) (b) and the ZrB_2 matrix (bright phase) (c). No grain boundaries was observed neither in the ZrB_2 matrix nor in the ZrC_xN_{1-x} rods, implying that the ZrC_xN_{1-x} rods were single-crystalline and grown in a single-crystalline ZrB_2 matrix. The ZrC_xN_{1-x} rods were hexagonally faceted and the rectilinear boundary of the hexagonal facets corresponded to $\{\bar{2}11\}$ planes (Fig. 6(a)). The diffraction patterns shown in Figs. 6(b) and (c) were taken from a specimen at different tilt angles (with several degrees difference). The zone axis of ZrC_xN_{1-x} [111] was almost parallel to that of ZrB_2 [0001]. Sorrell *et al*. reported that the interfacial orientation relationship in the ZrB_2-ZrC lamellar eutectic was ZrB_2 (0001)//ZrC (111).[21] In our unpublished work, an in-plane orientation relationship in the arc-melted ZrB_2-ZrN rod-like eutectic composite was found to be ZrB_2 (0001)//ZrN (111). The crystal orientation relationship of {111}//{0001} was very common between cubic and hexagonal crystal structures because of lattice matching.[16, 21, 26-30] The deviation between the two zone axes of ZrB_2 [0001] and ZrC_xN_{1-x} [111] might be caused by the fluctuation of the eutectic growth conditions. No obvious effect of the ZrC_xN_{1-x} composition on the crystal orientation relationship between the ZrB_2 single-crystalline matrix and the ZrC_xN_{1-x} single-crystalline rods was observed. Fig. 7 shows an illustration of the atomic alignment of the ZrC_xN_{1-x} {111} plane along $ZrC_xN_{1-x} < 111 >$ direction. Since ZrC_xN_{1-x} had a NaCl-type structure, the Zr atoms on the ZrC_xN_{1-x} {111} plane were hexagonally close-packed with the hexagonal facet corresponding to {211} plane. This was in consistent with the hexagonally faceted structure of ZrC_xN_{1-x} rods shown in Fig. 6(a).

Figure 8 shows a bright-field TEM image of the longitudinal section of the ZrB_2–ZrC_xN_{1-x} rod-like eutectic structure (a), the corresponding SAED patterns of the ZrC_xN_{1-x} rods (b) and the interface region between the ZrB_2 matrix and the ZrC_xN_{1-x} rods (c). The single-crystalline ZrC_xN_{1-x} rods were aligned to the growth direction, about 8.5 degrees to the $[1\bar{1}1]$ direction. The zone axis of ZrC_xN_{1-x} $[10\bar{1}]$ in Fig. 8 (b) was parallel to that of ZrB_2 $[2\bar{1}\bar{1}0]$ in Fig. 8 (c). In addition, the ZrC_xN_{1-x} (111) was parallel to ZrB_2 $(02\bar{2}0)$ as indicated in Fig. 8(c). Therefore, the crystal orientation relationship between the single-crystalline ZrB_2 matrix and the single-crystalline ZrC_xN_{1-x} rods in the rod-like eutectic structure was ZrB_2 $\{01\bar{1}0\}$//ZrC_xN_{1-x} $\{111\}$ and $ZrB_2 < 2\bar{1}\bar{1}0 >$//$ZrC_xN_{1-x} < 10\bar{1} >$. However, in the arc-melted TiB_2–TiC_xN_{1-x} rod-like eutectic structure, a different crystal orientation relationship of $TiB_2 < 0001 >$//$TiC_xN_{1-x} < 111 >$ and TiB_2 $\{11\bar{2}0\}$//TiC_xN_{1-x} $\{\bar{2}02\}$ was observed between the TiB_2 matrix and the TiC_xN_{1-x} rods.[26] The crystal orientation relationship between phases in the floating zone-melted ZrB_2–ZrC lamellar eutectic structure was $ZrB_2 < \bar{1}210 >$//$ZrC < 01\bar{1} >$ and ZrB_2 $\{0001\}$ // ZrC $\{111\}$, which was the same as that found in the arc-melted TiB_2–TiC_xN_{1-x} rod-like eutectic structure.[21,26] As shown in Fig. 8, the growth direction of the ZrC_xN_{1-x} rods was close to ZrC_xN_{1-x} $[1\bar{1}1]$ and the angle between ZrB_2 [0001] and ZrC_xN_{1-x} $[1\bar{1}1]$ was about 20 degrees. The eutectic growth direction shown in Fig. 8 was different from that depicted in Fig. 6, where ZrB_2 [0001] was almost parallel to ZrC_xN_{1-x} [111]. Therefore there were multiple crystal orientation relationships between the ZrB_2 matrix and the ZrC_xN_{1-x} rods. Fig. 9(a) presents a bright-field TEM image of the end of a ZrC_xN_{1-x} rod and Fig. 9(b) depicts a high-resolution TEM image of the designated area b in Fig. 9(a). The interface between ZrB_2 and ZrC_xN_{1-x} was wavy and clean, and no impurity phases were observed.

The dependence of the Vickers hardness of the arc-melted ZrB_2–ZrC–ZrN composites on ZrB_2 content (ZrC/ZrN=1:1) is depicted in Fig. 10. The applied indentation loads were 2 N and 5 N, respectively. The H_V increased first and then decreased with increasing ZrB_2 content. It reached the maximum at ZrB_2 content of 50 mol%. The $50ZrB_2$–25ZrC–25ZrN composite with a rod-like eutectic structure showed the highest H_V value of 18.6 GPa (indentation load: 2 N). The hardening effect could be attributed to the small grain size of

the rod-like eutectic structure. The hardness of 2 N indentation was higher than that of 5 N indentation, but they showed similar trend with increasing ZrB_2 content. The H_V value of the ZrB_2–ZrC_xN_{1-x} composites was lower than that of a dense ZrB_2–ZrC_x composite (about 20 GPa at indentation load of 5 N) produced by reactive hot pressing, because the grain sizes of the ZrB_2 and ZrC_x were much smaller (about 0.6 and 0.4 μm, respectively) than that of ZrB_2 and ZrC_xN_{1-x} in this study.[31] Another reason for the discrepancy was that ZrB_2 and ZrC were reported to be harder than ZrN.[12-13, 32] The hardness of the directionally solidified ZrB_2-ZrC lamellar eutectics were reported to have a maximum Knoop hardness of 24 GPa at an indentation load of 4.9 N.[33] The hardness of the ZrB_2-ZrC lamellar eutectics exhibited the classical Hall-Petch behavior with interlamellar spacing in the range of 1.85 to 2.75 μm.[33] However, it was difficult to compare Knoop hardness with Vickers hardness due to the different propensities for cracking and different sensitivities to load and indenter geometry.[34] A concomitant increase in Vickers hardness with decreasing microstructural scale, a near-linear relationship rather than a traditional Hall-Petch relationship, was observed in a laser irradiation produced B_4C-TiB_2 lamellar eutectic ceramic composite, which reached a high Vickers hardness of 32 GPa (indentation load: 9.81 N) at an interlamellar spacing of 0.18 μm.[35]

The Vickers hardness of the rod-like eutectic composites with 50 mol% ZrB_2 increased slightly with increasing C/N ratio as shown in Fig. 11. As mentioned above, the diameter of the ZrC_xN_{1-x} rods slightly increased with increasing C/N ratio. Classically, a decrease in Vickers hardness value would be expected for larger grain sizes according to the Hall-Petch equation.[36] The hardness of the ZrB_2 matrix would not change with the ZrC_xN_{1-x} fractions. Thus, the increase in hardness with composition was due to the increase in hardness from the solid solution of ZrC_xN_{1-x} phase. The hardness of ZrC_xN_{1-x} would increase with the x value since ZrC had a higher hardness than ZrN.[12-13] The evolution of the hardness of the rod-like eutectic composites with 50 mol% ZrB_2 could be the result of two competing mechanisms: the Hall-Petch relationship and rule-of-mixtures law, and generally followed a rule-of-mixtures type of behavior.

Fig. 12 shows the load dependence of the Vickers hardness of the $50ZrB_2$–$50ZrC_xN_{1-x}$ (the tested composite was $50ZrB_2$–40ZrC–10ZrN) eutectic composite. At indentation loads

less than 10 N, the Vickers hardness was load-dependent and decreased linearly with increasing applied load. At indentation loads greater than 10 N, the Vickers hardness became constant with an abrupt transition to a constant value about 15 GPa. Low indentation loads were associated with deformation, whereas fracture was more prominent at high indentation loads, in which the cracking might influence the hardness of one material that had cracked.[34] Similarly, a plateau in the hardness-load curve was observed in the laser processed B_4C-TiB_2 lamellar eutectic composite with an interlamellar spacing of 0.35 μm.[35] The Vickers hardness–load curves for typical brittle ceramics, such as Al_2O_3, Si_3N_4 and α-SiC, also exhibited a distinct transition to a plateau hardness level that corresponded to a relationship among hardness, Young's modulus and fracture toughness.[34]

4. Conclusions

ZrB_2–ZrC_xN_{1-x} quasi-binary eutectic composites were prepared by arc-melting ZrB_2, ZrC and ZrN powders in an N_2 astrosphere. The composites consisted of ZrB_2 and ZrC_xN_{1-x} two phases and showed a rod-like eutectic structure at a nominal composition of 50 mol% of ZrB_2, irrespective of the ZrC/ZrN ratio. In the ZrB_2–ZrC_xN_{1-x} rod-like eutectic structures, single-crystalline ZrC_xN_{1-x} rods were grown in single-crystalline ZrB_2 matrices. Of the two crystal orientation relationships observed between phases in the ZrB_2–ZrC_xN_{1-x} eutectic composites, one was determined as ZrB_2 $\{01\bar{1}0\}$//ZrC_xN_{1-x} $\{111\}$ and ZrB_2 $<2\bar{1}\bar{1}0>$//ZrC_xN_{1-x} $<10\bar{1}>$. The Vickers hardness of the ZrB_2–ZrC_xN_{1-x} rod-like eutectic composite was load-dependant at low indentation loads (less than 10 N) and was higher than that of the hypo- and hypereutectic composites. The $50ZrB_2$–40ZrC–10ZrN (mol%) eutectic composite showed the highest Vickers hardness of 19 GPa at an indentation load of 2 N.

Acknowledgement

This study was supported by Tohoku University, Japan and the MEXT (Ministry of Education, Culture, Sports, Science and Technology), Scientific Research (B) No.

25289223. Eric Jianfeng Cheng thanks the financial support from the China Scholarship Council, P.R.China. Eric Jianfeng Cheng would also like to thank Dr. Robert Schmidt for proofreading the manuscript.

Reference

1. E. Wuchina, E. Opila, M. Opeka, W. Fahrenholtz, and I. Talmy, "UHTCs: ultra-high temperature ceramic materials for extreme environment applications," *Electrochem. Soc. Interface.,* 16[4] 30 (2007).

2. W. G. Fahrenholtz, G. E. Hilmas, I. G. Talmy, and J. A. Zaykoski, "Refractory diborides of zirconium and hafnium," *J. Am. Ceram. Soc.,* 90[5] 1347-64 (2007).

3. M. W. Bird, T. Rampton, D. Fullwood, P. F. Becher, and K. W. White, "Local dislocation creep accommodation of a zirconium diboride silicon carbide composite," *Acta Mater.,* 84[0] 359-67 (2015).

4. V. Medri, F. Monteverde, A. Balbo, and A. Bellosi, "Comparison of ZrB_2-ZrC-SiC Composites Fabricated by Spark Plasma Sintering and Hot Pressing," *Advanced Engineering Materials,* 7[3] 159-63 (2005).

5. J. Adachi, K. Kurosaki, M. Uno, and S. Yamanaka, "Porosity influence on the mechanical properties of polycrystalline zirconium nitride ceramics," *Journal of Nuclear Materials,* 358[2–3] 106-10 (2006).

6. M. F. Ashby, "Criteria for selecting the components of composites," *Acta Metallurgica et Materialia,* 41[5] 1313-35 (1993).

7. A. Sayir and S. C. Farmer, "The effect of the microstructure on mechanical properties of directionally solidified $Al_2O_3/ZrO_2(Y_2O_3)$ eutectic," *Acta Mater.,* 48[18–19] 4691-97 (2000).

8. Y. Waku, N. Nakagawa, T. Wakamoto, H. Ohtsubo, K. Shimizu, and Y. Kohtoku, "High-temperature strength and thermal stability of a unidirectionally solidified Al_2O_3/YAG eutectic composite," *J. Mater. Sci.,* 33[5] 1217-25 (1998).

9. Y. Waku, N. Nakagawa, T. Wakamoto, H. Ohtsubo, K. Shimizu, and Y. Kohtoku, "A ductile ceramic eutectic composite with high strength at 1,873 K," *Nature,* 389[6646] 49-52 (1997).

10. C. C. Sorrell, V. S. Stubican, and R. C. Bradt, "Mechanical properties of ZrC-ZrB_2 and ZrC-TiB_2

directionally solidified eutectics " *J. Am. Ceram. Soc.,* 69[4] 317-21 (1986).

11. C. M. Chen, L. T. Zhang, W. C. Zhou, Z. Z. Hao, Y. J. Jiang, and S. L. Yang, "Microstructure, mechanical performance and oxidation mechanism of boride in situ composites," *Composites Science and Technology,* 61[7] 971-75 (2001).

12. S. S. Ordan'yan and V. I. Unrod, "Reactions in the system ZrC-ZrB_2," *Soviet Powder Metallurgy and Metal Ceramics,* 14[5] 393-95 (1975).

13. S.S.Ordan'yan and V.D.Chupov, "Interaction in ZrN-ZrB_2 and HfN-HfB_2 systems," *Inorganic Materials* 20[12] 1719 (1985).

14. I. Danisina, R. Avarbe, Y. A. Omel'chenko, and T. Ryzhkova, "Phase diagram of the system zirconium-zirconium nitride-zirconium carbide," *Zh. Prikl. Khim., 41: 492-500 (1968).* (1968).

15. E. J. Cheng, H. Katsui, R. Tu, and T. Goto, "Rod-like eutectic structure of arc-melted TiB_2–TiC_xN_{1-x} composite," *J. Eur. Ceram. Soc.,* 34[9] 2089-94 (2014).

16. D. Vallauri, I. Adrián, and A. Chrysanthou, "TiC–TiB_2 composites: A review of phase relationships, processing and properties," *J. Eur. Ceram. Soc.,* 28[8] 1697-713 (2008).

17. E. J. F. Cheng, H. Katsui, and T. Goto, "Lamellar and Rod-Like Eutectic Growth of TiB_2-TiC-TiN Composites by Arc-Melting," pp. 43-46 in Key Engineering Materials. Vol. 616.

18. K. Momma and F. Izumi, "VESTA: a three-dimensional visualization system for electronic and structural analysis," *J. Appl. Crystallogr.,* 41[3] 653-58 (2008).

19. K. Nakamura and M. Yashima, "Crystal structure of NaCl-type transition metal monocarbides MC (M= V, Ti, Nb, Ta, Hf, Zr), a neutron powder diffraction study," *Materials Science and Engineering: B,* 148[1] 69-72 (2008).

20. K. Aigner, W. Lengauer, D. Rafaja, and P. Ettmayer, "Lattice parameters and thermal expansion of Ti (C_xN_{1-x}), Zr (C_xN_{1-x}), Hf (C_xN_{1-x}) and TiN_{1-x} from 298 to 1473 K as investigated by high-temperature X-ray diffraction," *J. Alloys. Compd.,* 215 121-26 (1994).

21. C. Sorrell, H. Beratan, R. Bradt, and V. Stubican, "Directional Solidification of (Ti, Zr) Carbide-(Ti, Zr) Diboride Eutectics," *J. Am. Ceram. Soc.*, 67[3] 190-94 (1984).

22. A. Parisi and M. Plapp, "Stability of lamellar eutectic growth," *Acta Mater.*, 56[6] 1348-57 (2008).

23. S. Liu, J. H. Lee, and R. Trivedi, "Dynamic effects in the lamellar–rod eutectic transition," *Acta Mater.*, 59[8] 3102-15 (2011).

24. F. Schmid and D. Viechnicki, "Oriented eutectic microstructures in the system Al_2O_3/ZrO_2," *J. Mater. Sci.*, 5[6] 470-73 (1970).

25. S. Bourban, N. Karapatis, H. Hofmann, and W. Kurz, "Solidification microstructure of laser remelted Al_2O_3-ZrO_2 eutectic," *Acta Mater.*, 45[12] 5069-75 (1997).

26. E. J. Cheng, H. Katsui, R. Tu, and T. Goto, "Long-Range Ordered Structure of Ti–B–C–N in a TiB_2–TiC_xN_{1-x} Eutectic Composite," *J. Am. Ceram. Soc.*, 97 [8] 2423-26 (2014).

27. J. Y. Dai, Y. G. Wang, D. X. Li, and H. Q. Ye, "Atomic structure at Ti(C,N)-TiB_2 interfaces in Ti(C,N)-TiB_2-Ni ceramics," *Philos. Mag. A*, 70[5] 905-16 (1994).

28. F. Mei, N. Shao, L. Wei, Y. Dong, and G. Li, "Coherent epitaxial growth and superhardness effects of *c*-TiN/*h*-TiB_2 nanomultilayers," *Appl. Phys. Lett.*, 87[1] 011906-06-3 (2005).

29. J. Y. Dai, D. X. Li, H. Q. Ye, G. J. Zhang, and Z. Z. Jin, "Characterization of TiB_2-Ti(CN)-Ni ceramics by transmission and analytical electron microscopy," *Mater.Lett*, 16[6] 317-21 (1993).

30. H. Holleck, C. Kühl, and H. Schulz, "Wear resistant carbide–boride composite coatings," *J. Vac. Sci. Technol. A*, 3[6] 2345-47 (1985).

31. L. Rangaraj, S. J. Suresha, C. Divakar, and V. Jayaram, "Low-Temperature Processing of ZrB_2-ZrC Composites by Reactive Hot Pressing," *Metallurgical and materials transactions A*, 39[7] 1496-505 (2008).

32. C. Chen, C. Liu, and C. Y. A. Tsao, "Influence of growth temperature on microstructure and mechanical properties of nanocrystalline zirconium carbide films," *Thin Solid Films*, 479[1–2] 130-36 (2005).

33. C. C. Sorrell, V. S. Stubican, and R. C. Bradt, "Mechanical Properties of ZrC-ZrB_2 and ZrC-TiB_2

Directionally Solidified Eutectics," *J. Am. Ceram. Soc.*, 69[4] 317-21 (1986).

34. J. Quinn and G. D Quinn, "Indentation brittleness of ceramics: a fresh approach," *J. Mater. Sci.*, 32[16] 4331-46 (1997).

35. R. M. White, J. M. Kunkle, A. V. Polotai, and E. C. Dickey, "Microstructure and hardness scaling in laser-processed B_4C–TiB_2 eutectic ceramics," *J. Eur. Ceram. Soc.*, 31[7] 1227-32 (2011).

36. E. Hall, "The deformation and ageing of mild steel: III discussion of results," *Proceedings of the Physical Society. Section B*, 64[9] 747 (1951).

Figure captions

Fig. 1 Prepared nominal compositions (indicated by black dots) of mixtures of the ZrB_2, ZrC and ZrN starting powders

Fig. 2 XRD pattern of the arc-melted $50ZrB_2$–30ZrC–20ZrN (mol%) composite

Fig. 3 SEM micrographs of the arc-melted ZrB_2–ZrC–ZrN composites: (a) $30ZrB_2$–50ZrC–20ZrN, (b) $40ZrB_2$–40ZrC–20ZrN, (c) $60ZrB_2$–20ZrC–20ZrN, (d) $80ZrB_2$–10ZrC–10ZrN (mol%)

Fig. 4 SEM micrographs of the arc-melted ZrB_2–ZrC–ZrN rod-like eutectic composites: (a) $50ZrB_2$–10ZrC–40ZrN, (b) $50ZrB_2$–25ZrC–25ZrN, (c) $50ZrB_2$–30ZrC–20ZrN, (d) $50ZrB_2$–40ZrC–10ZrN (mol%)

Fig. 5 Backscattered electron SEM micrograph of the arc-melted $50ZrB_2$–30ZrC–20ZrN composite (mol%)

Fig. 6 Bright-field TEM image of the transverse section of the ZrB_2–ZrC_xN_{1-x} rod-like eutectic structure (a); SAED pattern of the of ZrC_xN_{1-x} rods (b); SAED pattern of the ZrB_2

matrix (c). The diffraction patterns shown in (b) and (c) were taken from a sample at different tilt angles (with several degrees difference)

Fig. 7 Illustration of the atomic alignment of $ZrC_xN_{1-x}\{111\}$ lattice plane along ZrC_xN_{1-x} $< 111 >$ direction

Fig. 8 Bright-field TEM image of the longitudinal section of the ZrB_2–ZrC_xN_{1-x} rod-like eutectic structure (a); SAED pattern of the of ZrC_xN_{1-x} rods (b); SAED pattern of the interface region between the ZrB_2 matrix and the ZrC_xN_{1-x} rod (c)

Fig. 9 (a) bright-field TEM image of the end of a ZrC_xN_{1-x} rod; high-resolution TEM image of the designated area b in (a)

Fig. 10 Dependence of the Vickers hardness of the arc-melted ZrB_2–ZrC–ZrN composites on ZrB_2 content (ZrC/ZrN=1:1, indentation loads: 2 N and 5 N, respectively)

Fig. 11 Dependence of the Vickers hardness of the $50ZrB_2$–$50ZrC_xN_{1-x}$ (mol%) composites on C/N ratio (indentation load: 2 N; the inset of Fig. 11 showing the top-view of an indentation impression of $50ZrB_2$–40ZrC–10ZrN (mol%) composite)

Fig. 12 Load dependence of the Vickers hardness of the $50ZrB_2$–$50ZrC_xN_{1-x}$ (mol%) composites

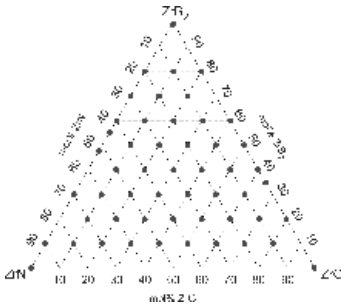

jace_13984_f1.tif

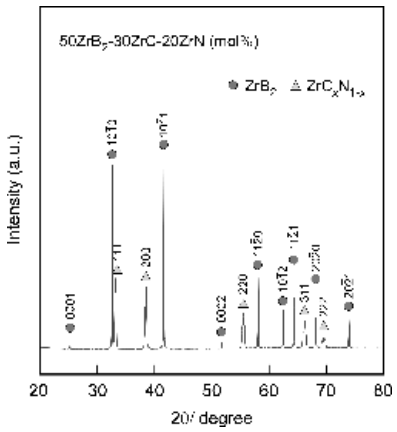

jace_13984_f2.tif

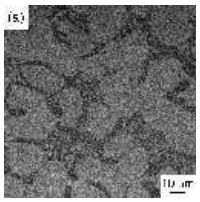

jace_13984_f3a.tif

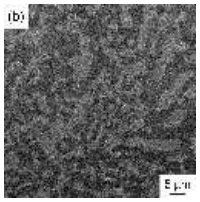

jace_13984_f3b.tif

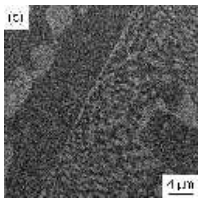

jace_13984_f3c.tif

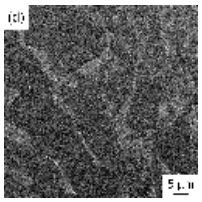

jace_13984_f3d.tif

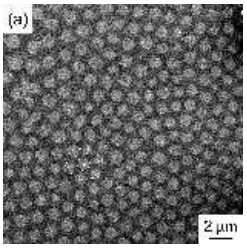

jace_13984_f4a.tif

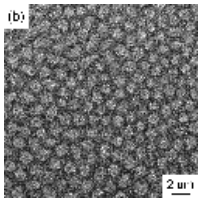

jace_13984_f4b.tif

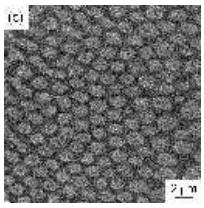

jace_13984_f4c.tif

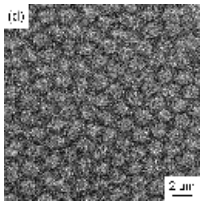

jace_13984_f4d.tif

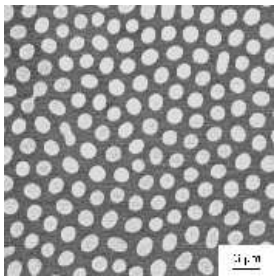

jace_13984_f5.tif

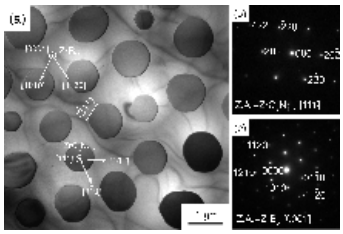

jace_13984_f6.tif

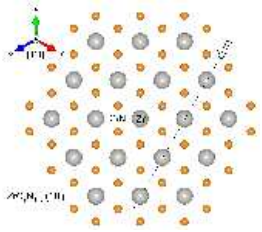

jace_13984_f7.tif

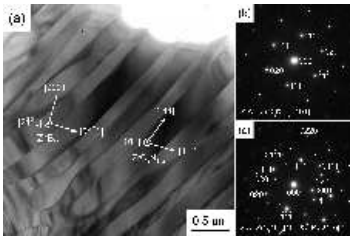

jace_13984_f8.tif

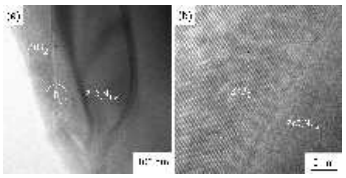

jace_13984_f9.tif

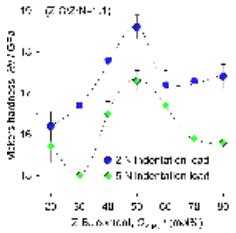

jace_13984_f10.tif

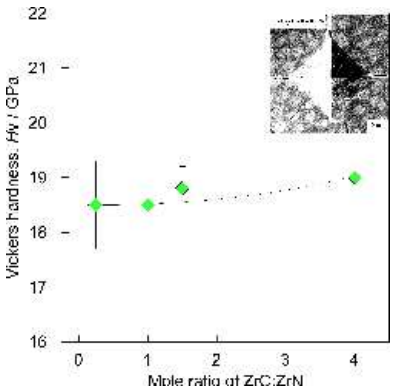

jace_13984_f11.tif

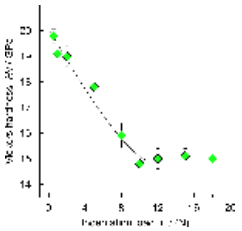

jace_13984_f12.tif